

Resummation-based Quantum Monte Carlo for Entanglement Entropy Computation

Menghan Song,¹ Ting-Tung Wang,¹ and Zi Yang Meng^{1,*}

¹*Department of Physics and HKU-UCAS Joint Institute of Theoretical and Computational Physics,
The University of Hong Kong, Pokfulam Road, Hong Kong SAR, China*

(Dated: October 4, 2023)

Based on the recently developed resummation-based quantum Monte Carlo method for the $SU(N)$ spin and loop-gas models, we develop a new algorithm, dubbed ResumEE, to compute the entanglement entropy (EE) with greatly enhanced efficiency. Our ResumEE converts the evaluation of the exponentially small value of the $\langle e^{-S^{(2)}} \rangle$, where $S^{(2)}$ is the 2nd order Rényi EE, to an important sampling process with polynomial accuracy such that the $S^{(2)}$ for a generic 2D quantum $SU(N)$ spin models can be readily computed without facing the exponential explosion of its variance. We benchmark our algorithm with the previously proposed estimators of $S^{(2)}$ on 1D and 2D $SU(2)$ Heisenberg spin systems to reveal its superior performance and then use it to detect the entanglement scaling data of the Néel-to-VBS transition on 2D $SU(N)$ Heisenberg model with continuously varying N . Our ResumEE algorithm solves the critical problem of precisely evaluating the quantum entanglement in many-body systems and will have a significant impact on reliable access to the conformal field theory data for the highly entangled quantum matter.

Introduction.— The $SU(N)$ spin [1–3] and loop-gas [4–9] models, especially at the large- N limit, are theoretically important and have been intensively investigated over the years [10–12]. From the numerical side, there have been significant developments in the quantum Monte Carlo (QMC) simulation techniques to solve such models [3, 13–20]. Based on the valence-bond basis [17], a few projection QMC works tried to determine the phase transition from the antiferromagnetic (AFM) Néel state to the valence bond solid (VBS) state as the N in $SU(N)$ increases [16]. The finite temperature path-integral QMC algorithm has also been developed [13, 14] and many interesting phase transitions, especially when further interactions beyond the nearest-neighbor have been included, are subsequently discovered [18–21], similar discoveries are also made in the loop-gas models [4–9]. These efforts have culminated in the recent discovery that the deconfined quantum criticality (DQC) in its $SU(N)$ spin model realization (J_1 - J_2 $SU(N)$ model on square lattice with spins in the fundamental representation on sub-lattice A and the conjugate representation on sub-lattice B) will only be recovered when $N \geq 7$ from the entanglement entropy (EE) measurement [22].

The Entanglement entropy, as a non-local quantum measurement, follows the scaling form of "area law" [23–25]. The corrections to the area law usually contain universal information [26–33] and can be used to identify quantum phases [34–37] and phase transitions [22, 30–33, 38–40] in lattice model simulations. QMC simulations of Rényi entanglement entropy offer the ability to probe these fundamental properties in large system sizes and higher dimensions by interpreting the Rényi entropies from partition functions of replicated space-time manifolds [27, 41–44]. It is in the work of EE computation in $SU(N)$ J_1 - J_2 spin model [22], that we find although the existing EE computation algorithms can efficiently access Rényi entropy of $SU(N)$ spin models at

small N [30, 37, 45, 46], the simulations become cumbersome when N is large, with larger auto-correlation time and noisier data compared with their $SU(2)$ or $SU(3)$ cousins. The basic problem is that the configuration space in the Monte Carlo sampling process becomes exponentially large as N increases, i.e., each site has N local degrees of freedom, such that traditional stochastic series expansion (SSE) operator loop update [17, 47] has to deal with too many types (N colors) of loops, making it exponentially hard to visit all the configurations, compared with, for example, the $SU(2)$ case. Due to this difficulty, one cannot even compute the local observables, such as the magnetization and VBS order parameters accurately at large- N , let alone non-local observables, such as EE where one needs to replicate the partition function, and whose evaluation $\langle e^{-S^{(2)}} \rangle$ where $S^{(2)}$ is the 2nd order Rényi EE could render exponential explosion of its variance [48, 49].

Apparently, a new QMC updated scheme is needed to reduce the complexity introduced by the multi-color loops in the $SU(N)$ or loop-gap models, and recently, there appears to be such a scheme that serves the purpose [50]. In the resummation-based QMC method, as schematically shown in Fig. 1, Desai and Pujari introduced the finite- T operator-loop updates which directly handle uncolored loops without any reference to the underlying spin states and, therefore, manage to re-sum all the contributions from numerous colored loops into one single uncolored loop. This method works well in medium-to-large N cases and, more importantly, inspires us to develop a more efficient sampling algorithm for the EE computation in the $SU(N)$ quantum spin models, dubbed ResumEE – resummation-based quantum Monte Carlo for entanglement entropy computation.

In this work, we develop the ResumEE and demonstrate its capability to tackle generic $SU(N)$ spin models at *continuous* N . Benefiting from the compact configu-

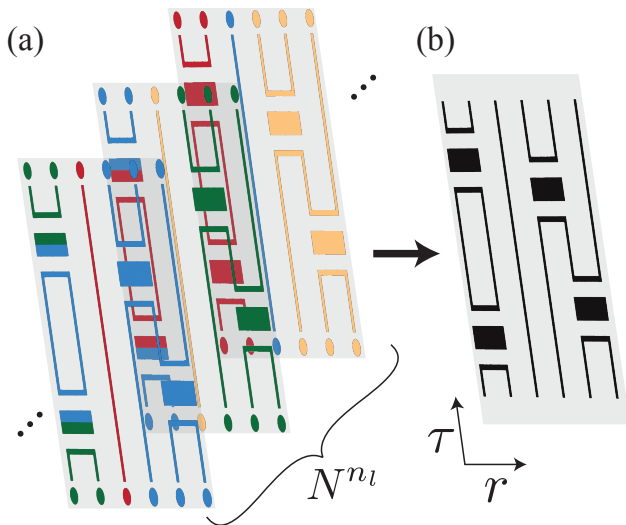


FIG. 1. **Concept sketch for the resummation QMC.** In this example, $N^{n_l=4}$ colored spin configurations with the same loop structure (panel (a)) for a general $SU(N)$ model are resummed into a compact uncolored loop configuration (panel (b)). In the coordinate, r stands for the spatial direction of the lattice, and the τ is the imaginary time direction in the partition function.

ration space, we find that not only at large- N but also in the well-studied $SU(2)$ case, our algorithm greatly improves the previous EE computation methods, such as those in Refs. [27, 43, 44] in both 1D and 2D cases. Therefore, the ResumEE algorithm successfully mitigates the long-standing issue of the exponential explosion of EE's variance, which has plagued most of the previous EE estimators in QMC [26, 27, 42–44, 51–53].

We first benchmark our algorithm with previously proposed estimators of EE [27, 43, 44] on 1D and 2D $SU(2)$ Heisenberg spin systems to reveal its superior performance and then use it to detect the entanglement scaling data of the Néel-to-VBS transition on 2D $SU(N)$ Heisenberg model on a square lattice with *continuously* varying N . Our results reveal that although previous work suggested there is a continuous transition at $N_c \approx 4.57(5)$ [16], the more sensitive EE computation finds out that the transition is actually weakly- first-order with a substantial log-correction to the area law scaling in EE when the entanglement region has a smooth boundary. Such a log-correction, we believe, is inherited from the domains that exhibit $SU(N)$ continuous symmetry-breaking with gapless Goldstone modes, which coexist with the VBS domains at their weakly- first-order transition point. Once pushed to substantially larger system sizes, our local order parameter measurements convey the same message of phase coexistence of the Néel and VBS states.

The ResumEE algorithm, therefore, not only demonstrates its superior performance compared with the

previous EE computation schemes but offers a sensitive non-local probe that could distinguish the fundamental information of the transition that is otherwise very difficult for conventional probes. We, therefore, believe our ResumEE makes an essential step towards solving the critical problem of precisely evaluating the quantum entanglement in many-body systems and is of unusual intrinsic interest to a broad audience from condensed matter to quantum information and computation.

Resummation QMC and traditional EE estimators.—In the path-integral QMC, traditionally, one can series expand the partition function as

$$\begin{aligned} Z(\beta) &= \text{Tr}\{e^{-\beta H}\} \\ &= \sum_{n=0}^{\infty} \frac{(-\beta)^n}{n!} \sum_{\{b_m, \mu_m\}} \sum_{\sigma} \langle \sigma | H_{b_1, \mu_1} H_{b_2, \mu_2} \cdots H_{b_n, \mu_n} | \sigma \rangle \end{aligned} \quad (1)$$

where $\{b_m, \mu_m\}$ identifies the m -th operator at bond b_m in the operator string with operator type μ_m (diagonal or off-diagonal) and $|\sigma\rangle$ is the basis state the operators H_{b_m, μ_m} are operated upon (usually it is the product state of the on-site $|S_i^z\rangle$). For the $SU(N)$ spin model, typical configurations of Eq. (1), are shown in Fig. 1 (a), one can image the operator loops as closely packed colored loops [54]. And since there are N colors, the total number of configurations is exponentially large, i.e., N^{n_l} , where n_l is the number of loops.

The resummation QMC [50] sums over the spin or color indices of these closely packed loops without changing loop connections along the operator string, such that colored configurations that share the same loop connection, as shown in Fig. 1 (a), are compressed into one uncolored loop configuration in Fig. 1 (b). The simplified partition function is now

$$Z(\beta) = \sum_{n=0}^{\infty} \frac{(-\beta)^n}{n!} N^{n_l} \sum_{\{b_n\}} h_{b_1} h_{b_2} \cdots h_{b_n}, \quad (2)$$

where one only needs to record the operator position b_m . In our $SU(N)$ Hamiltonian, $h_{b_m} = -\frac{J}{N}$ is the spin-symmetric matrix element, and n_l is the number of loops in a given configuration. We emphasize that the uncolored nature of the loops emerges in the presence of $SU(N)$ symmetry, and the diagonal and off-diagonal operators in Eq. (1) contribute the same element in Eq. (2). Another interesting observation is that the symmetry index N is now a parameter that can be tuned continuously instead of only the integer in its original form.

Based on such a resummation scheme of the partition function of the $SU(N)$ Hamiltonian in Eq. (2), we can discuss the computation of the entanglement entropy based on the evaluation of the partition function ratio on different space-time manifolds [23, 42, 43]. Here, we use

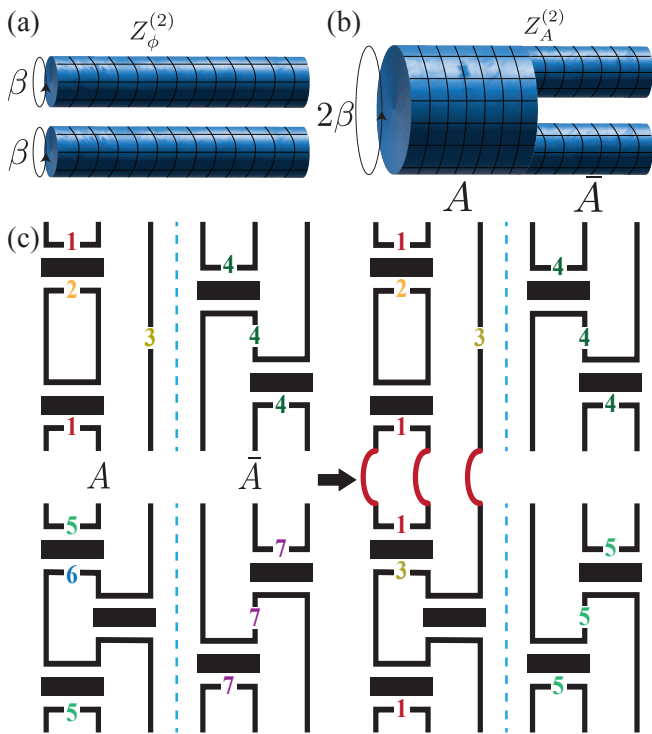


FIG. 2. **The resummation-based EE computation.** Panel (a) shows the independent ensemble of two replicas corresponding to the partition function $Z_\phi^{(2)}$, and panel (b) shows the ensemble where the entanglement region A is glued with imaginary time-periodic boundary condition 2β , corresponding to partition function $Z_A^{(2)}$. The environment \bar{A} , still has the boundary condition of β . Panel (c) shows an example of measuring $\langle P_{\emptyset \rightarrow A} \rangle$ in ResumEE algorithm.

the second order Rényi EE as an example. As shown in Fig. 2, for a quantum many-body system, the EE with entanglement region A can be expressed as

$$S_A^{(2)} = -\ln \frac{Z_A^{(2)}}{Z_\phi^{(2)}} = -\ln \frac{\langle P_{\emptyset \rightarrow A} \rangle}{\langle P_{A \rightarrow \emptyset} \rangle}, \quad (3)$$

and the two partition functions $Z_\phi^{(2)}$ and $Z_A^{(2)}$ are computed on the two different space-time manifolds in Fig. 2 (a) and (b), respectively. The last equality in Eq. (3) is achieved because we define the probabilities $\langle P_{\emptyset \rightarrow A} \rangle$ and $\langle P_{A \rightarrow \emptyset} \rangle$ as

$$\begin{aligned} \langle P_{X \rightarrow \bar{X}} \rangle &= \frac{Z_{X \cap \bar{X}}^{(2)}}{Z_X^{(2)}} = \frac{\sum_{C \in X \cap \bar{X}} W(C)}{\sum_{C \in X} W(C)} \\ &= \frac{\sum_{C \in X} W(C) \delta_{\bar{X}}(C)}{\sum_{C \in X} W(C)} = \langle \delta_{\bar{X}}(C) \rangle_X, \end{aligned} \quad (4)$$

and

$$\delta_X(C) = \begin{cases} 1, & \text{if } C \in X \\ 0, & \text{if } C \notin X \end{cases}, \quad (5)$$

where X and \bar{X} are dummy variables being \emptyset and A interchangeably and $W(C)$ is the configurational weight for configuration C specified in the partition function Eq. (2).

In Eq. (4), when $C \in \emptyset$, the Monte Carlo average is carried out in the space-time manifolds such that the loop configurations are on the two independent replicas as in Fig. 2 (a); and when $C \in A$, the loop configurations are on the manifold with the entanglement region A connected/glued but the environment \bar{A} are independent, as in Fig. 2 (b). For computing $\langle P_{\emptyset \rightarrow A} \rangle$, the $C \in \emptyset \cap A$ in the numerator in Eq. (4) means that although we sample in the two independent replicas, i.e., $C \in \emptyset$, we need to count the spin configurations that satisfy the periodic boundary condition of the glued manifold of $C \in A$, hence the δ_A function; and vice versa for $\langle P_{A \rightarrow \emptyset} \rangle$.

In the traditional path-integral QMC estimator of EE [42, 43], one measures δ_X by comparing the spins in A at the imaginary time boundaries. If all the spins satisfy the boundary condition of X , a 1 is recorded, and 0 otherwise. As already indicated in Ref. [42], such a counting method becomes inefficient when the entanglement region A is large since the ratio becomes exponentially small and the MC process becomes a sampling of rare events. Although later an improved version is introduced in Ref. [43] taking advantage of symmetry, measuring an exponentially small quantity by sampling 1s and 0s is still ill-conditioned, as one would need at least $e^{S_A^{(2)}}$ MC steps to get an average value of order $e^{-S_A^{(2)}}$. The computation cost scales exponentially with $S_A^{(2)}$ and hence the linear system size in 2D, as the leading term in EE is the area law $S_A^{(2)} \sim L$.

The ResumEE algorithm.—In the ResumEE, the situation is different. Here, one can effectively sample N^{n_l} spin configurations with each loop configuration. We can, therefore, sample a small but finite value of $\langle P_{A \rightarrow \emptyset} \rangle$ and $\langle P_{\emptyset \rightarrow A} \rangle$ each time instead of waiting for a 1 to appear indefinitely. To be more specific, the two probabilities $\langle P_{A \rightarrow \emptyset} \rangle$ and $\langle P_{\emptyset \rightarrow A} \rangle$ can be evaluated as the ratios of numbers of possible spin configurations under different boundary conditions. They can be measured with the reduction of the number of loops when one enforces the additional boundary condition, as the number of loops determines the number of possible spin configurations. That is,

$$P_{\emptyset \rightarrow A} = \frac{N^{n_{glued}}}{N^{n_1} N^{n_2}} = N^{n_{glued} - (n_1 + n_2)}, \quad (6)$$

where n_1 and n_2 are the numbers of loops in each independent replica, and n_{glued} is the number of loops when one glued them together in region A .

Fig. 2 (c) explicitly shows an example of measuring $P_{\emptyset \rightarrow A}$ according to Eq. (6). Before gluing the loops into the $C \in A$ manifold, one has $n_1 + n_2 = 7$. After applying

the additional boundary condition, one has $n_{glued} = 5$. Therefore, one sample a $P_{\emptyset \rightarrow A} = N^{-2}$ with this loop configuration, as opposed to sample a 1 every N^2 times if one were to measure with the original method with spin configurations. $P_{A \rightarrow \emptyset}$ can be measured in a similar manner, with the only difference being that the additional boundary condition is cast on the top and bottom of one of the replicas.

In practice, one only needs to count the number of distinct groups reduced at the boundary of imaginary time during such a gluing process, as the loops in the middle of time propagation will appear in both cases and cancel out in the ratio of partition functions, e.g., loops 2, 4 and 7 in Fig. 2 (c). Since the number of spin configurations measured in the resummation algorithm increases exponentially with system size, the ResumEE succeeded in overcoming the exponential decay in EE, or the exponential explosion of its variance [48, 49], as it happened in the previous methods [27, 43, 44]. We now turn to the results to demonstrate such superior performance.

Benchmark with $SU(2)$ Heisenberg model.— We consider the quantum spin model with Hamiltonian $H = -J \sum \langle i, j \rangle P_{ij}$, where the $SU(N)$ singlet projector is defined as $P_{ij} = \frac{1}{N} \sum_{\alpha, \beta} |\alpha_i \alpha_j\rangle \langle \beta_i \beta_j|$ with α, β ranging from 1 to N . The lattice is $d = (1, 2)$ dimension bipartite (in these cases, chain and square lattice) lattice such that the α spins are in the fundamental representation on one sub-lattice and β spins are in the conjugate representation on the other sub-lattice.

To benchmark the performance of the ResumEE algorithm, we first compute the second order Rényi EE of two well-known examples at $SU(2)$ cases, the spin-1/2 Heisenberg chain, and the spin-1/2 square lattice AFM Heisenberg model. The results are shown in Fig. 3. One sees in the 1D case (Fig. 3 (a)) that the ResumEE always has controlled errorbars as l_A (the entanglement region) increases, while the traditional EE estimators in Ref. [43] quickly experience the exponential explosion of the variance [27, 43, 44]. The contrast is even clearer in the 2D case in Fig. 3 (b). In this case, the square lattice $SU(2)$ antiferromagnetic model has spontaneous symmetry breaking Néel phase with $N_G = 2$ Goldstone modes at ground state, and since the entanglement region acquires smooth boundary (see the inset of Fig. 3 (b)), one expects the scaling behavior of $S_A^{(2)}(L) = aL + b \ln L + c$ with the leading area law and the universal coefficient $b = \frac{N_G(d-1)}{2} = 1$ in the sub-leading term [26, 37, 44, 46, 49] with $d = 2$ the spatial dimension. One sees that the ResumEE readily captures the expected scaling behavior, but the traditional EE estimators cannot offer precise values for $L = 14, 16$, and cannot sample a value for $L > 16$ for the CPU hour we used since none of $\langle P_{A \rightarrow \emptyset} \rangle$ or $\langle P_{\emptyset \rightarrow A} \rangle$

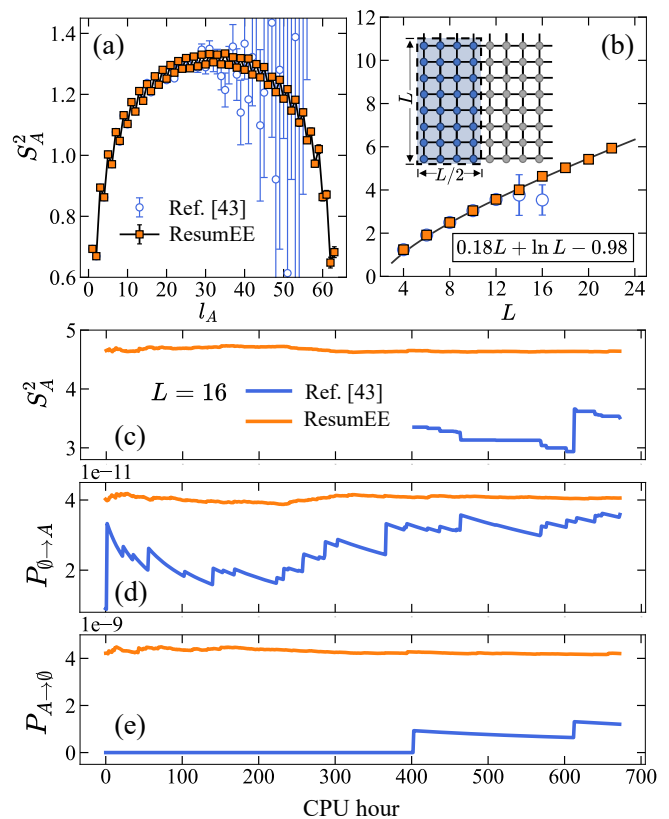


FIG. 3. Benchmark $S_A^{(2)}$ for 1D and 2D $SU(2)$ Heisenberg model. (a) Comparison of our ResumEE method and previous EE estimator in Ref. [43] on a 1D Heisenberg chain with $L = 64$ and inverse temperature $\beta = 128$. The size of the entanglement region is l_A . (b) Comparison of ResumEE and EE estimator in Ref. [43] on 2D $SU(2)$ square lattice with $L = 4, 6, \dots, 16$ and $\beta = L$. The entanglement region A is of size $L \times L/2$ with a smooth boundary of length $l_A = 2L$. In all cases, we perform the same amount of CPU hours for fair comparison. In (a), it is obvious that when $l_A > L/2$, the traditional EE results experience the exponential explosion of variance, whereas the ResumEE has controlled errors. In (b), only the ResumEE can yield the expected scaling of $S_A^{(2)}(L) = aL + b \ln L + c$, where $b = \frac{N_G}{2} = 1$ with $N_G = 2$ the number of Goldstone modes in the Néel phase of AFM $SU(2)$ Heisenberg model on square lattice. Panels (c) (d) and (d) demonstrate the convergence of S_A^2 , $P_{\emptyset \rightarrow A}$ and $P_{A \rightarrow \emptyset}$ against simulation time at $L = 16$ in panel (b), respectively.

measurements find spin configurations with satisfactory boundary conditions. At $L = 16$, one can see in panel (c)-(e) that the measurables obtained in ResumEE converge much faster than those sampled using the traditional method in Ref. [43]. The traditional method actually failed to sample any effective value of $P_{A \rightarrow \emptyset}$ until 400 CPU hours (Fig. 2 (e)), so no EE data was recorded (Fig. 2 (c)). To make a fair comparison, we have purposely kept the same amount of CPU hours for the ResumEE and traditional EE estimator in all the data of Fig. 3.

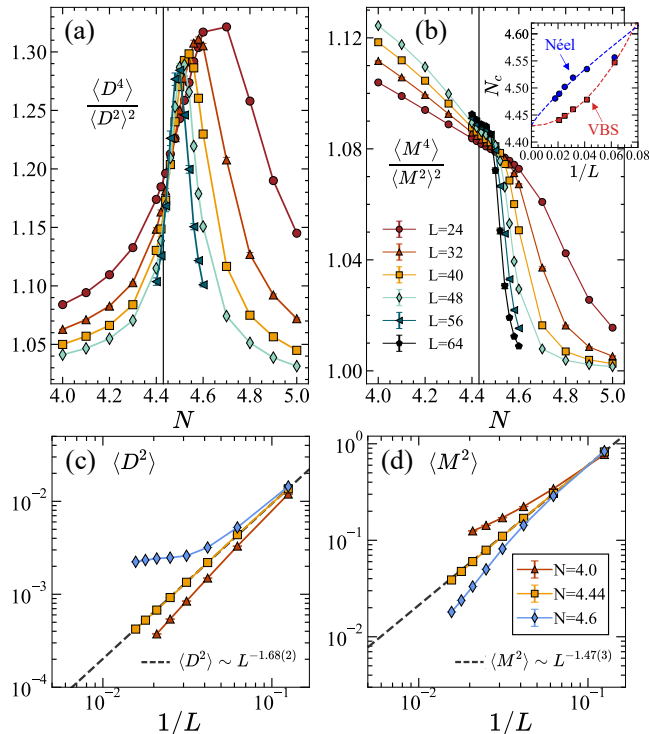


FIG. 4. **Determine Néel-VBS transition in the SU(N) model from local probes.** Panels (a) and (b) demonstrate the Binder ratio crossing of VBS and Néel order parameters, respectively. The inset in (b) shows the convergence to a common critical point of the two crossings as $L \rightarrow \infty$ and determines N_c . However, a clear coexistence region of both Néel and VBS orders is present in the finite size data and could well persist to the thermodynamic limit and will yield a weakly-first-order transition. Panels (c) and (d) demonstrate how the finite-size VBS and Néel order parameters vary as the system size inside two phases and near the transition point. Up to the present system sizes, one can see the scaling dimensions of the two order parameters are different.

Phase transition in the SU(N) Heisenberg model with continuously varying N .— Finally, we turn to the quantum phase transition in the SU(N) model as a function of continuously varying N . It is known that this model has a Néel ordered ground state at SU($N \leq 4$) while a VBS ground state at SU($N \geq 5$) [3, 14, 55]. Later, Ref. [16] with projection QMC of VBS basis suggested a continuous phase transition at $N_c \approx 4.57(5)$ separating the Néel phase with onsite spin rotational symmetry breaking and the VBS phase with Z_4 lattice symmetry breaking. This finding is interesting because the transition, if continuous, shares the flavors of deconfined quantum criticality (DQC) in that two spontaneously symmetry-breaking phases meet at a single critical point with one tuning parameter. Although we have to acknowledge that the present case is different from the DQC in that the symmetry of the Hamiltonian changes when N changes, the

Néel-VBS transition in the present case could nevertheless offer new ingredients of novel quantum phase transitions.

However, previous analysis of the continuous phase transition [16] assumes that both the Néel and VBS phases share the same anomalous dimension, i.e., $\eta_N = \eta_V$. It was reported later that η_N deviates from η_V in the SU(N) DQC scenario with $N > 2$, and $\eta_N = \eta_V$ is a special case for SU(2) [19]. Although our case is not identical to the DQC scenario, it is reasonable to investigate the critical N_c more carefully without a priori assumption such as $\eta_N = \eta_V$. Also, the previous results are based on the projection QMC at the ground state. With the resummation QMC in the path-integral, we can simulate larger system sizes (up to $L = 64$) than those in Ref. [16]. So, we decided to examine the Néel-VBS transition point in a more accurate manner.

We solve the problem from two different directions. First, we adopt the traditional practice by looking into the local order parameters for Néel and VBS phases and use the traditional finite-size scaling analysis to locate the more accurate critical region and the transition point. These results are shown in Fig. 4. We choose the M^2 (square of magnetization) as the square of the Néel order parameter, which is defined as the expectation value of the projection operator, $\frac{1}{L^4} \sum_{\mathbf{r}, \mathbf{r}'} P_{\mathbf{r}, \mathbf{r}'}$. And, components of VBS order parameter $\mathbf{D} = (D_x, D_y)$ are defined as $D_a = \frac{1}{L^2} \sum_{\mathbf{r}} (-1)^{r_a} P_{\mathbf{r}, \mathbf{r} + \hat{\mathbf{e}}_a}$ with a being x or y . We choose the $D^2 = D_x^2 + D_y^2$ (square of the dimerization) as the square of the VBS order parameter. The raw data of $\langle D^2 \rangle$ and $\langle M^2 \rangle$ are given in Appendix A.

One sees from Fig. 4 (a) and (b) that both the Binder ratios of $\frac{\langle M^4 \rangle}{\langle M^2 \rangle^2}$ and $\frac{\langle D^4 \rangle}{\langle D^2 \rangle^2}$ have crossing points for various system sizes. The crossings of both Binder ratios eventually meet at a single point, $N_c = 4.43(2)$ at the thermodynamic limit, $L \rightarrow \infty$, as shown in the inset of Fig. 4 (b). A critical point near $N_c = 4.43$ can also be seen from the scaling of order parameters as a function of system sizes. One can see from Fig. 4 (c) and (d) that at $N = 4.44 \approx N_c$ both $\langle D^2 \rangle$ and $\langle M^2 \rangle$ vanish in power law of system sizes, indicating a phase transition, although we note the exponents in the power law, namely, $\langle D^2 \rangle \sim L^{-1.68(2)}$ and $\langle M^2 \rangle \sim L^{-1.47(3)}$, are different and it means that the in this case, $\eta_N \neq \eta_V$. Another special point of the transition is that in the inset of Fig. 4 (b), one sees the crossing points of Néel and VBS phases at each finite size actually develop coexist behavior, and up to $L = 64$ in the coexistence region, i.e., as a function of N close to $N_c = 4.43$, the system has both Néel and VBS long-range order, and such coexistence could well persist in the thermodynamic limit. Such behavior is, in fact, reminiscent of a weakly-first-order transition, which can not be answered definitely with the measurement of local observables, even though our L is already larger than the previous work.

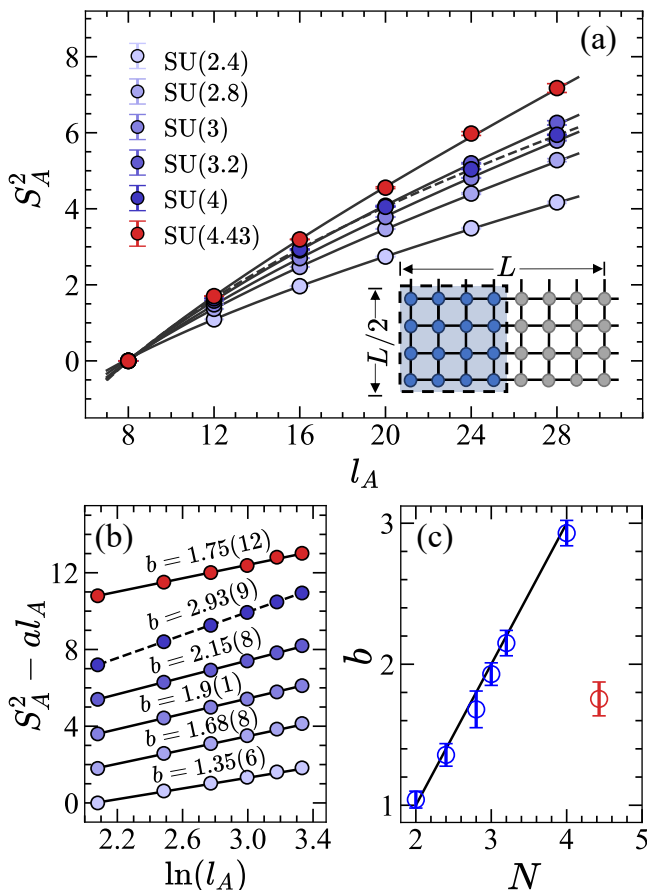


FIG. 5. **Scaling of entanglement entropy at different N in the $SU(N)$ model.** Panel (a) shows $S_A^2(l_A)$ obtained from the ResumEE method with smooth boundary at the transition point $N_c = 4.43$ determined from the Binder ratio crossings in Fig. 4. A clear sub-leading logarithmic correction is seen with the coefficient $b = 1.75(12)$ (panel (b)). We also show the EE for $SU(2.4)$, $SU(2.8)$, $SU(3)$, $SU(3.2)$ and $SU(4)$, these systems are well inside the Néel phase with $N_G = 2(N - 1)$ Goldstone modes, such that their sub-leading logarithmic corrections yields $b = \frac{N_G}{2} = N - 1$, as $b = 1.35(6)$, $1.68(8)$, $1.9(1)$, $2.15(8)$, $2.93(9)$ for the $SU(2.4)$, $SU(2.8)$, $SU(3)$, $SU(3.2)$ and $SU(4)$ cases in panel (b). Note that for $SU(4)$, we consider the $J_1 - J_2$ Hamiltonian (dashed line in (a) and (b)) to enhance the Néel order without changing universal information. Panel (c) summarizes the obtained b with respect to N , and the black line is $b = N - 1$ according to the Goldstone modes inside the $SU(N)$ symmetry-breaking phase. The red dot is the b for $SU(4.43)$, which represents the coexistence of the Néel state with the VBS state at the transition point. Therefore, the transition is actually of first-order.

This is where the non-local EE measurement comes to rescue. We study the scaling behavior of the $S_A^{(2)}$ at the transition point, $N_c = 4.43$ using ResumEE, and we utilize the incremental trick by gradually increasing the entanglement region to improve the data quality [30, 37, 41, 48, 49]. Detailed implementation of the

incremental protocol is described in Appendix B. First, We bi-partition systems with size $L \times L/2$ such that the entanglement region A acquires a smooth boundary with length $l_A = L$ and keep $\beta = L$. For a continuous phase transition described by a unitary CFT, there should be no log-correction to the leading area law at the QCP with a smooth boundary [26, 56]. In Fig. 5, we can clearly see for $N = 4.43$ a large and positive log coefficient $b = 1.93(4)$, deviating from the CFT constraint. With current knowledge, such log-correction emerged in smooth boundary cut could come from spontaneous continuous symmetry broken with $b = \frac{N_G(d-1)}{2}$. Therefore, such a finite b observed at $N_c = 4.43$ points towards a weakly-first-order phase transition with the co-existence of both Néel and VBS order parameters, which is hard to detect at finite system sizes with local observables.

In order to strengthen our argument, we also investigate the EE scaling inside the Néel phase, $N < N_c$. Note that as N approaches N_c , the finite-size effect in EE scaling becomes stronger. We introduce an extra next-nearest neighbor J_2 term, $-\frac{J_2}{N} \sum_{\langle\langle ij \rangle\rangle} |\beta_i \alpha_j| \langle \alpha_i \beta_j \rangle$ to the $SU(N)$ Heisenberg model at $SU(4)$ case to reduce the finite-size effect. J_2 term is the $SU(N)$ generalization of the next-nearest-neighbor ferromagnetic interaction and, therefore, enhances the Néel order while keeping universal information, such as the number of Goldstone modes, N_G , intact. In $SU(4)$ case (shown as a dashed line in Fig. 5), we set $J_2 = 3.5$ and use the non-equilibrium incremental algorithm [30, 37, 46], an efficient method to compute EE with further spin interactions other than J_1 . As shown in Fig. 5 (b), staying deep inside the Néel phase, we successfully detect the correct number of Goldstone modes $N_G = 2(N - 1)$ at $SU(3)$ and $SU(4)$ from EE scaling with the log coefficient, $b = 1.9(1)$ and $2.93(9)$ respectively. More interestingly, our ResumEE results find the consistency of $N_G = 2(N - 1)$ at non-integer N cases, $N = 2.4, 2.8, 3.2$ with $b = 1.35(6), 1.68(8), 2.15(8)$ respectively, as shown in Fig. 5 (c). This is another novel result from ResumEE that the CFT prediction of the log-correction can be analytically continued to non-integer N s, or in other words, the number of Goldstone modes N_G can also be fractionalized. Therefore, with the observation inside the Néel ordered phase, the finite log-correction at N_c serves as a clue of continuous symmetry-breaking right at this point, eventually pointing to a weakly-first-order phase transition.

We also note that the system sizes in Fig. 5 are smaller than those of the order parameter measurements in Fig. 4. This again shows that the non-local measurement, such as the EE and disorder operator [33, 57–59], are more sensitive in probing the subtle yet fundamental information of the nature of the phase transitions.

Discussion.—The precise computation of the EE for quantum many-body systems is the long-standing obsta-

cle that blockades our full-fledged exploration of the fundamental entanglement and CFT information of quantum matter. In the continuous efforts over the past two decades, various estimators of EE all suffered from the exponential explosion of its variances when the entanglement region just starts to scale [26, 27, 42–44, 48, 49, 51–53]. In this work, based on the recently developed resummation-based quantum Monte Carlo method for the $SU(N)$ spin and loop-gas models [50], we develop a new algorithm – ResumEE – manage to overcome the long-standing obstacle. Our ResumEE converts the evaluation of the exponentially small value of the $\langle e^{-S_A^{(2)}} \rangle$, into an important sampling process with polynomial accuracy such that the $S_A^{(2)}$ for a generic quantum $SU(N)$ spin models can be readily computed without facing the exponential explosion of its variance.

We demonstrate the superior performance of our algorithm over the previous estimators of $S_A^{(2)}$ on 1D and 2D $SU(2)$ Heisenberg spin systems. More importantly, we use it to detect the entanglement scaling data of the Néel-VBS transition on 2D $SU(N)$ Heisenberg model on a square lattice with *continuously* varying N . Our EE results reveal that although previous work suggested there is a continuous transition at $N_c \approx 4.57(5)$ [16], the transition is actually weakly-first-order with a substantial log-correction to the area law scaling in EE when the entanglement region has a smooth boundary. Such log-correction comes from the domains that exhibit $SU(N)$ continuous symmetry-breaking with gapless Goldstone modes, which coexist with the VBS domains at their weakly-first-order transition. Our local order parameter measurements convey the same message of phase coexistence of the Néel and VBS states once pushed to much larger system sizes. Our ResumEE also reveals a non-trivial phenomenon: the log-corrections of EE inside the Néel phase at non-integer N also follow the CFT prediction, leading to the fractionalization of Goldstone modes.

The ResumEE algorithm, therefore, not only demonstrates its superior performance compared with the previous EE QMC estimators but offers a sensitive non-local probe that could distinguish the fundamental information of the transition that is otherwise very difficult for conventional probes, as has also been shown in a few recent works where EE and similar non-local measurements offer similar sensitivity [22, 30–33, 37, 57–59]. We, therefore, believe our ResumEE makes an essential step towards solving the critical problem of precisely evaluating the quantum entanglement in many-body systems and is of unusual intrinsic interest to a broad audience from condensed matter to quantum information and computation.

Acknowledgments.—We acknowledge the inspiring discussions with Jiarui Zhao, Gaopei Pan, and YuanDa Liao. We thank the support from the Research Grants

Council (RGC) of Hong Kong Special Administrative Region (SAR) of China (Projects Nos. 17301420, 17301721, AoE/P-701/20, 17309822 and HKU C7037-22G), the ANR/RGC Joint Research Scheme sponsored by the RGC of Hong Kong SAR of China and French National Research Agency (Project No. A_HKU703/22) and the HKU Seed Funding for Strategic Interdisciplinary Research “Many-body paradigm in quantum moiré material research”. The authors also acknowledge the Tianhe-II platform at the National Supercomputer Center in Guangzhou, the HPC2021 system under the Information Technology Services and the Blackbody HPC system at the Department of Physics, University of Hong Kong, for their technical support and generous allocation of CPU time.

* zymeng@hku.hk

- [1] N. Read and S. Sachdev, Some features of the phase diagram of the square lattice $SU(N)$ antiferromagnet, *Nuclear Physics B* **316**, 609 (1989).
- [2] N. Read and S. Sachdev, Large- N expansion for frustrated quantum antiferromagnets, *Phys. Rev. Lett.* **66**, 1773 (1991).
- [3] N. Kawashima and Y. Tanabe, Ground States of the $SU(N)$ Heisenberg Model, *Phys. Rev. Lett.* **98**, 057202 (2007).
- [4] F. Alet, G. Misguich, V. Pasquier, R. Moessner, and J. L. Jacobsen, Unconventional Continuous Phase Transition in a Three-Dimensional Dimer Model, *Phys. Rev. Lett.* **97**, 030403 (2006).
- [5] D. Charrier and F. Alet, Phase diagram of an extended classical dimer model, *Phys. Rev. B* **82**, 014429 (2010).
- [6] A. Nahum, J. T. Chalker, P. Serna, M. Ortuño, and A. M. Somoza, 3D Loop Models and the CP^{n-1} Sigma Model, *Phys. Rev. Lett.* **107**, 110601 (2011).
- [7] A. Nahum, J. T. Chalker, P. Serna, M. Ortuño, and A. M. Somoza, Phase transitions in three-dimensional loop models and the CP^{n-1} sigma model, *Phys. Rev. B* **88**, 134411 (2013).
- [8] A. Nahum, J. T. Chalker, P. Serna, M. Ortuño, and A. M. Somoza, Deconfined Quantum Criticality, Scaling Violations, and Classical Loop Models, *Phys. Rev. X* **5**, 041048 (2015).
- [9] G. J. Sreejith, S. Powell, and A. Nahum, Emergent $SO(5)$ Symmetry at the Columnar Ordering Transition in the Classical Cubic Dimer Model, *Phys. Rev. Lett.* **122**, 080601 (2019).
- [10] R. K. Kaul and S. Sachdev, Quantum criticality of $U(1)$ gauge theories with fermionic and bosonic matter in two spatial dimensions, *Phys. Rev. B* **77**, 155105 (2008).
- [11] S. M. Chester, E. Dupuis, and W. Witczak-Krempa, Evidence for web of dualities from monopole operators, *Phys. Rev. D* **108**, L021701 (2023).
- [12] M. A. Metlitski, M. Hermele, T. Senthil, and M. P. A. Fisher, Monopoles in CP^{N-1} model via the state-operator correspondence, *Phys. Rev. B* **78**, 214418 (2008).
- [13] N. Kawashima and J. E. Gubernatis, Loop Algorithms

- for Monte Carlo Simulations of Quantum Spin Systems, *Phys. Rev. Lett.* **73**, 1295 (1994).
- [14] K. Harada, N. Kawashima, and M. Troyer, Néel and Spin-Peierls Ground States of Two-Dimensional $SU(N)$ Quantum Antiferromagnets, *Phys. Rev. Lett.* **90**, 117203 (2003).
- [15] F. F. Assaad, Phase diagram of the half-filled two-dimensional $SU(N)$ Hubbard-Heisenberg model: A quantum Monte Carlo study, *Phys. Rev. B* **71**, 075103 (2005).
- [16] K. S. D. Beach, F. Alet, M. Mambrini, and S. Capponi, $SU(N)$ Heisenberg model on the square lattice: A continuous- N quantum Monte Carlo study, *Phys. Rev. B* **80**, 184401 (2009).
- [17] A. W. Sandvik and H. G. Evertz, Loop updates for variational and projector quantum Monte Carlo simulations in the valence-bond basis, *Phys. Rev. B* **82**, 024407 (2010).
- [18] R. K. Kaul, Quantum criticality in $SU(3)$ and $SU(4)$ antiferromagnets, *Phys. Rev. B* **84**, 054407 (2011).
- [19] R. K. Kaul and A. W. Sandvik, Lattice Model for the $SU(N)$ Néel to Valence-Bond Solid Quantum Phase Transition at Large N , *Phys. Rev. Lett.* **108**, 137201 (2012).
- [20] K. Harada, T. Suzuki, T. Okubo, H. Matsuo, J. Lou, H. Watanabe, S. Todo, and N. Kawashima, Possibility of deconfined criticality in $SU(N)$ Heisenberg models at small N , *Phys. Rev. B* **88**, 220408 (2013).
- [21] M. S. Block, R. G. Melko, and R. K. Kaul, Fate of $\mathbb{C}\mathbb{P}^{N-1}$ Fixed Points with q Monopoles, *Phys. Rev. Lett.* **111**, 137202 (2013).
- [22] M. Song, J. Zhao, L. Janssen, M. M. Scherer, and Z. Y. Meng, Deconfined quantum criticality lost, *arXiv e-prints*, [arXiv:2307.02547](https://arxiv.org/abs/2307.02547) (2023).
- [23] P. Calabrese and J. Cardy, Entanglement entropy and quantum field theory, *Journal of Statistical Mechanics: Theory and Experiment* **2004**, P06002 (2004).
- [24] E. Fradkin and J. E. Moore, Entanglement Entropy of 2D Conformal Quantum Critical Points: Hearing the Shape of a Quantum Drum, *Phys. Rev. Lett.* **97**, 050404 (2006).
- [25] N. Laflorencie, Quantum entanglement in condensed matter systems, *Physics Reports* **646**, 1 (2016), quantum entanglement in condensed matter systems.
- [26] M. A. Metlitski and T. Grover, Entanglement Entropy of Systems with Spontaneously Broken Continuous Symmetry, *arXiv e-prints*, [arXiv:1112.5166](https://arxiv.org/abs/1112.5166) (2011).
- [27] D. J. Luitz, X. Plat, F. Alet, and N. Laflorencie, Universal logarithmic corrections to entanglement entropies in two dimensions with spontaneously broken continuous symmetries, *Phys. Rev. B* **91**, 155145 (2015).
- [28] N. Laflorencie, D. J. Luitz, and F. Alet, Spin-wave approach for entanglement entropies of the $J_1 - J_2$ Heisenberg antiferromagnet on the square lattice, *Phys. Rev. B* **92**, 115126 (2015).
- [29] D. J. Luitz and N. Laflorencie, Quantum Monte Carlo detection of $SU(2)$ symmetry breaking in the participation entropies of line subsystems, *SciPost Phys.* **2**, 011 (2017).
- [30] J. Zhao, Y.-C. Wang, Z. Yan, M. Cheng, and Z. Y. Meng, Scaling of Entanglement Entropy at Deconfined Quantum Criticality, *Phys. Rev. Lett.* **128**, 010601 (2022).
- [31] Y. D. Liao, G. Pan, W. Jiang, Y. Qi, and Z. Y. Meng, The teaching from entanglement: 2D $SU(2)$ antiferromagnet to valence bond solid deconfined quantum critical points are not conformal, *arXiv e-prints*, [arXiv:2302.11742](https://arxiv.org/abs/2302.11742) (2023).
- [32] M. Song, J. Zhao, Y. Qi, J. Rong, and Z. Y. Meng, Quantum criticality and entanglement for 2d long-range Heisenberg bilayer, [arXiv:2306.05465](https://arxiv.org/abs/2306.05465).
- [33] Z. H. Liu, Y. Da Liao, G. Pan, M. Song, J. Zhao, W. Jiang, C.-M. Jian, Y.-Z. You, F. F. Assaad, Z. Y. Meng, and C. Xu, Disorder Operator and Rényi Entanglement Entropy of Symmetric Mass Generation, *arXiv e-prints*, [arXiv:2308.07380](https://arxiv.org/abs/2308.07380) (2023).
- [34] S. V. Isakov, M. B. Hastings, and R. G. Melko, Topological entanglement entropy of a Bose-Hubbard spin liquid, *Nature Physics* **7**, 772 (2011).
- [35] H.-C. Jiang, Z. Wang, and L. Balents, Identifying topological order by entanglement entropy, *Nature Physics* **8**, 902 (2012).
- [36] M. S. Block, J. D’Emidio, and R. K. Kaul, Kagome model for a \mathbb{Z}_2 quantum spin liquid, *Phys. Rev. B* **101**, 020402 (2020).
- [37] J. Zhao, B.-B. Chen, Y.-C. Wang, Z. Yan, M. Cheng, and Z. Y. Meng, Measuring Rényi entanglement entropy with high efficiency and precision in quantum Monte Carlo simulations, *npj Quantum Materials* **7**, 69 (2022).
- [38] B. Swingle and T. Senthil, Structure of entanglement at deconfined quantum critical points, *Phys. Rev. B* **86**, 155131 (2012).
- [39] S. Inglis and R. G. Melko, Entanglement at a two-dimensional quantum critical point: a $T = 0$ projector quantum Monte Carlo study, *New Journal of Physics* **15**, 073048 (2013).
- [40] A. B. Kallin, K. Hyatt, R. R. P. Singh, and R. G. Melko, Entanglement at a Two-Dimensional Quantum Critical Point: A Numerical Linked-Cluster Expansion Study, *Phys. Rev. Lett.* **110**, 135702 (2013).
- [41] M. B. Hastings, I. González, A. B. Kallin, and R. G. Melko, Measuring Renyi Entanglement Entropy in Quantum Monte Carlo Simulations, *Phys. Rev. Lett.* **104**, 157201 (2010).
- [42] S. Humeniuk and T. Roscilde, Quantum Monte Carlo calculation of entanglement Rényi entropies for generic quantum systems, *Phys. Rev. B* **86**, 235116 (2012).
- [43] D. J. Luitz, X. Plat, N. Laflorencie, and F. Alet, Improving entanglement and thermodynamic Rényi entropy measurements in quantum Monte Carlo, *Phys. Rev. B* **90**, 125105 (2014).
- [44] B. Kulchytsky, C. M. Herdman, S. Inglis, and R. G. Melko, Detecting Goldstone modes with entanglement entropy, *Phys. Rev. B* **92**, 115146 (2015).
- [45] V. Alba, Out-of-equilibrium protocol for Rényi entropies via the Jarzynski equality, *Phys. Rev. E* **95**, 062132 (2017).
- [46] J. D’Emidio, Entanglement Entropy from Nonequilibrium Work, *Phys. Rev. Lett.* **124**, 110602 (2020).
- [47] A. W. Sandvik and H. G. Evertz, Loop updates for variational and projector quantum Monte Carlo simulations in the valence-bond basis, *Phys. Rev. B* **82**, 024407 (2010).
- [48] Y. D. Liao, Controllable Incremental Algorithm for Entanglement Entropy and Other Observables with Exponential Variance Explosion in Many-Body Systems, *arXiv e-prints*, [arXiv:2307.10602](https://arxiv.org/abs/2307.10602) (2023).
- [49] G. Pan, Y. D. Liao, W. Jiang, J. D’Emidio, Y. Qi, and Z. Y. Meng, Stable computation of entanglement entropy for two-dimensional interacting fermion systems, *Phys. Rev. B* **108**, L081123 (2023).
- [50] N. Desai and S. Pujari, Resummation-based quantum Monte Carlo for quantum paramagnetic phases, *Phys.*

- [Rev. B **104**, L060406 \(2021\)](#).
- [51] F. F. Assaad, T. C. Lang, and F. Parisen Toldin, Entanglement spectra of interacting fermions in quantum Monte Carlo simulations, [Phys. Rev. B **89**, 125121 \(2014\)](#).
 - [52] P. Broecker and S. Trebst, Numerical stabilization of entanglement computation in auxiliary-field quantum Monte Carlo simulations of interacting many-fermion systems, [Phys. Rev. E **94**, 063306 \(2016\)](#).
 - [53] C.-C. Chang, R. R. P. Singh, and R. T. Scalettar, Entanglement properties of the antiferromagnetic-singlet transition in the Hubbard model on bilayer square lattices, [Phys. Rev. B **90**, 155113 \(2014\)](#).
 - [54] R. K. Kaul, Marshall-positive $SU(N)$ quantum spin systems and classical loop models: A practical strategy to design sign-problem-free spin Hamiltonians, [Phys. Rev. B **91**, 054413 \(2015\)](#).
 - [55] N. Kawashima and K. Harada, Recent Developments of World-Line Monte Carlo Methods, [Journal of the Physical Society of Japan **73**, 1379 \(2004\)](#).
 - [56] J. Helmes and S. Wessel, Entanglement entropy scaling in the bilayer Heisenberg spin system, [Phys. Rev. B **89**, 245120 \(2014\)](#).
 - [57] Y.-C. Wang, N. Ma, M. Cheng, and Z. Y. Meng, Scaling of the disorder operator at deconfined quantum criticality, [SciPost Phys. **13**, 123 \(2022\)](#).
 - [58] Z. H. Liu, W. Jiang, B.-B. Chen, J. Rong, M. Cheng, K. Sun, Z. Y. Meng, and F. F. Assaad, Fermion Disorder Operator at Gross-Neveu and Deconfined Quantum Criticalities, [Phys. Rev. Lett. **130**, 266501 \(2023\)](#).
 - [59] W. Jiang, B.-B. Chen, Z. H. Liu, J. Rong, F. F. Assaad, M. Cheng, K. Sun, and Z. Y. Meng, Many versus one: The disorder operator and entanglement entropy in fermionic quantum matter, [SciPost Phys. **15**, 082 \(2023\)](#).

Appendix A: QMC data for order parameters

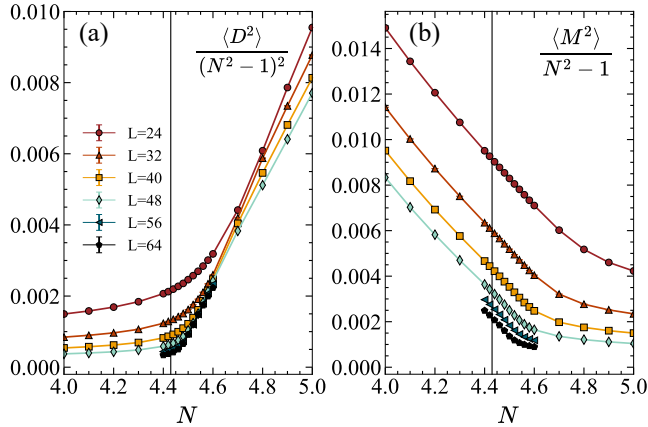


FIG. 1. QMC data for Néel and VBS order parameters. Panels (a) ((b)) show VBS (Néel) order parameters of various system sizes against N . The black line indicates the transition point N_c extrapolated in Fig. 4 in the main text.

Fig. 1 shows the expectation value of the square of the order parameters for both VBS $\langle D^2 \rangle$ and Néel phases $\langle M^2 \rangle$ of various system sizes against N . Since the number of components of the order parameter varies as N changes, we investigate one component of both order parameters by including a normalization factor to better visualize their behavior across the transition. We can see from Fig. 1 (a) and (b) that both order parameters tend to vanish near $N_c = 4.43$ (black line), which is also evidence of phase transition at N_c determined in the main text. We find our finite size results of $\langle M^2 \rangle$ are consistent with those in Ref. [16], as the scale of Fig. 1 (b). But as discussed in the main, once zoom in to the transition region, there are subtle differences in obtaining the location of the N_c .

Appendix B: Incremental approach of EE computation

Instead of calculating the probabilities $\langle P_{\emptyset \rightarrow A} \rangle$ and $\langle P_{A \rightarrow \emptyset} \rangle$ directly, the Rényi entanglement entropy $e^{-S_A^{(2)}}$

can also be broken down into smaller pieces, that is,

$$\begin{aligned} e^{-S_A^{(2)}} &= \frac{Z_A}{Z_\emptyset} \\ &= \frac{Z_{A_n}}{Z_{A_{n-1}}} \frac{Z_{A_{n-1}}}{Z_{A_{n-2}}} \dots \frac{Z_{A_k}}{Z_{A_{k-1}}} \dots \frac{Z_{A_1}}{Z_{A_0}} \\ &= \frac{P_{A_{n-1} \rightarrow A_n}}{P_{A_n \rightarrow A_{n-1}}} \dots \frac{P_{A_{k-1} \rightarrow A_k}}{P_{A_k \rightarrow A_{k-1}}} \dots \frac{P_{A_0 \rightarrow A_1}}{P_{A_1 \rightarrow A_0}} \end{aligned} \quad (\text{B1})$$

where A_n is set to be A , and A_0 is set to be \emptyset . A_k are intermediate entanglement regions as shown in Fig. 2.

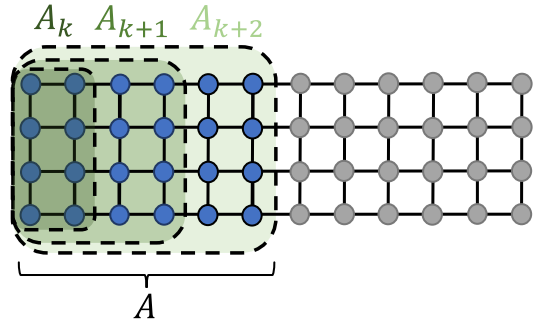


FIG. 2. Schematic of the incremental entanglement regions. A_k , A_{k+1} and A_{k+2} are the intermediate entanglement regions in which the ratio in Eq. (B1) are computed independently. Since the incremental regions are not very different from each other, the incremental ratios computed are well-conditioned, compared with direct computation of $\langle P_{\emptyset \rightarrow A} \rangle$ and $\langle P_{A \rightarrow \emptyset} \rangle$.

They are added so that each probability has a larger value and the statistical error can be suppressed.

In this study, we let each consecutive A_k be two columns wider than the former A_{k-1} .